

Low-carrier density and fragile magnetism in a Kondo lattice system

Binod K. Rai,¹ Iain W. H. Oswald,² Wenjing Ban,³ C.-L. Huang,^{1,*} V. Loganathan,¹ A. M. Hallas,^{1,4} M. N. Wilson,⁴ G. M. Luke,^{4,5,6} L. Harriger,⁷ Q. Huang,⁷ Y. Li,¹ Sami Dzsaber,⁸ Julia Y. Chan,² N. L. Wang,³ Silke Paschen,⁸ J. W. Lynn,⁷ Andriy H. Nevidomskyy,¹ Pengcheng Dai,¹ Q. Si,¹ and E. Morosan^{1,†}

¹*Department of Physics and Astronomy and Rice Center for Quantum Materials, Rice University, Houston, Texas 77005, USA*

²*Department of Chemistry, University of Texas at Dallas, Richardson, Texas 75080, USA*

³*International Center for Quantum Materials, School of Physics, Peking University, Beijing 100871, China*

⁴*Department of Physics and Astronomy, McMaster University, Hamilton, Ontario, Canada L8S 4M1*

⁵*Canadian Institute for Advanced Research, 661 University Ave, Suite 505, Toronto, Ontario, Canada M5G 1M1*

⁶*TRIUMF, 4004 Wesbrook Mall, Vancouver, B.C., Canada V6T 2A3*

⁷*NIST Center for Neutron Research, National Institute of Standards and Technology, Gaithersburg, Maryland 20899, USA*

⁸*Institute of Solid State Physics, Vienna University of Technology, Wiedner Hauptstrasse 8-10, 1040 Vienna, Austria*



(Received 20 August 2018; revised manuscript received 10 January 2019; published 12 February 2019)

Kondo-based semimetals and semiconductors are of extensive current interest as a viable platform for strongly correlated states in the dilute carrier limit. It is thus important to explore the routes to understand such systems. One established pathway is through the Kondo effect in metallic nonmagnetic analogs, in the so called half-filling case of one conduction electron and one $4f$ electron per site. Here, we demonstrate that Kondo-based semimetals develop out of conduction electrons with a low-carrier density in the presence of an even number of rare-earth sites. We do so by studying the Kondo material $\text{Yb}_3\text{Ir}_4\text{Ge}_{13}$ along with its closed- $4f$ -shell counterpart, $\text{Lu}_3\text{Ir}_4\text{Ge}_{13}$. Through magnetotransport, optical conductivity, and thermodynamic measurements, we establish that the correlated semimetallic state of $\text{Yb}_3\text{Ir}_4\text{Ge}_{13}$ below its Kondo temperature originates from the Kondo effect of a low-carrier conduction-electron background. In addition, it displays fragile magnetism at very low temperatures, which in turn, can be tuned to a Griffiths-phase-like regime through Lu-for-Yb substitution. These findings are connected with recent theoretical studies in simplified models. Our results can pave the way to exploring strong correlation physics in a semimetallic environment.

DOI: [10.1103/PhysRevB.99.085120](https://doi.org/10.1103/PhysRevB.99.085120)

I. INTRODUCTION

The proximity of the f energy level to the Fermi energy E_F in rare-earth compounds often causes hybridization of the local moments with the conduction electrons. The resulting Kondo effect gives rise to a broad range of electronic properties, from metallic heavy fermion (HF) systems to Kondo insulators, and intermediate low-carrier Kondo semiconductors or semimetals. Kondo systems have garnered much attention in recent years because of their exotic electronic and magnetic behavior, including quantum criticality, a breakdown of the Fermi-liquid picture, unconventional superconductivity, and topologically protected states [1–4]. Only a small number of $4f$ low-carrier HF systems have been reported so far, e.g., CeNiSn and CeRhSb [5,6], $\text{CeNi}_{2-\delta}\text{As}_2$ [7], and $\text{Ce}_3\text{Bi}_4\text{Pd}_3$ [8]. These compounds realize HF physics in a parameter regime that is separate from the canonical “half-filling” case, and thus alternative low-carrier Kondo systems are called for to broaden our knowledge in such a regime.

Our recent discovery of the six nonmagnetic germanides $\text{Y}_3\text{T}_4\text{Ge}_{13-x}$ ($T = \text{Ir, Rh, Os}$) and $\text{Lu}_3\text{T}_4\text{Ge}_{13-x}$

($T = \text{Co, Rh, Os}$) [9] pointed to a possible generalization of low-carrier behavior in these “3-4-13” germanides, due to the negative temperature coefficients of the electrical resistivity $\rho(T)$, i.e., $d\rho/dT < 0$, compared to the normal metal behavior ($d\rho/dT > 0$) in the stannide analogs [10]. Here, we report the discovery that the correlated semimetal $\text{Yb}_3\text{Ir}_4\text{Ge}_{13}$ (YbIG) [11] emerges from the Kondo effect in a nonmagnetic dilute-carrier system, $\text{Lu}_3\text{Ir}_4\text{Ge}_{13}$ (LIG). YbIG exhibits $d\rho/dT < 0$ in the whole measured temperature range from 300 to 0.1 K, including inside a fragile magnetic state below $T_{\text{mag}}^* = 0.9$ K. The underlying electronic properties of YbIG are dictated by its nonmagnetic analog LIG, which, remarkably, also shows semimetal-like behavior between 300 and 2.8 K, below which LIG becomes superconducting. This is in stark contrast with the metallic behavior found in the nonmagnetic analogs of other known Kondo semimetals [12–16]. Optical conductivity measurements and band-structure calculations reinforce the semimetal-like nature of YbIG and LIG. Moreover, the substitution of nonmagnetic Lu on the Yb site induces Griffiths-phase-like behavior, as evidenced by the power-law temperature dependence of the magnetic susceptibility M/H and magnetic specific heat C_{mag}/T at low T . The coexistence of the low-carrier density, the Kondo effect, and the associated semimetal behavior, as well as the fragile magnetism, makes YbIG one of the most complex f -electron systems. We rationalize our finding using

*clh@rice.edu

†emorosan@rice.edu

a recently developed framework of the Kondo-lattice effect in the dilute-carrier limit [17].

II. EXPERIMENTAL METHODS

Single crystals of $(\text{Yb}_{1-x}\text{Lu}_x)_3\text{Ir}_4\text{Ge}_{13}$ ($x = 0, 0.2, 0.4, 0.5, 0.55, 0.6, 0.7, 0.8, \text{ and } 1$) were prepared using a Ge self-flux method [9]. Structure determination was performed using single-crystal x-ray diffraction data collected on a Bruker D8 Quest diffractometer with a Mo-target $\text{I}\mu\text{S}$ microfocus x-ray tube. Powder x-ray diffraction patterns were collected with a Rigaku D/Max diffractometer using $\text{Cu } K\alpha$ radiation. Rietveld analysis was performed using the GSAS software package. The temperature-dependent ac resistivity of bar-shaped crystals was collected in the Quantum Design (QD) Physical Properties Measurement System (PPMS), with current $i \parallel a$. To measure the Hall coefficient, we applied a magnetic field perpendicular to the a axis and measured the transverse voltage. A reverse field was applied to cancel out longitudinal magnetoresistance contributions due to misalignment. dc magnetic susceptibility was measured in a QD Magnetic Properties Measurement System (MPMS) with a ^3He insert. Specific heat was collected in a QD PPMS with a ^3He insert using a thermal relaxation method. The optical reflectance measurements were performed on Bruker IFS 113v and 80v spectrometers in the frequency range from 30 to 45 000 cm^{-1} . An *in situ* gold and aluminum overcoating technique was used to obtain the reflectance $R_{\text{opt}}(\omega)$. The real part of conductivity $\sigma_1(\omega)$ is obtained by the Kramers-Kronig transformation of $R_{\text{opt}}(\omega)$. The Hagen-Rubens relation was used for low-frequency extrapolation; at the high-frequency side, a ω^{-1} relation was used up to 300 000 cm^{-1} , above which ω^{-4} was applied.

Neutron diffraction experiments were carried out on the BT-7 triple-axis spectrometer [18] and the BT-1 high-resolution powder diffractometer at NIST Center for Neutron Research (NCNR), Gaithersburg, Maryland. The samples were put into an annulus configuration to reduce the neutron absorption. Muon spin relaxation (μSR) measurements were performed on the M15 beamline at the TRIUMF laboratory. The advantage of this technique is that muons are extremely sensitive to their local magnetic environment [19]. A small 10 G longitudinal field was applied to decouple any relaxation from static nuclear dipoles. Several pieces of single crystal were affixed directly to the dilution refrigerator's silver cold finger using Apiezon N-grease. The muons that land outside the sample (in the silver sample holder or the cryostat tails) produce a temperature-independent contribution to the asymmetry. This temperature-independent component has been fitted and subtracted from the data, leaving only the asymmetry arising from muons that land in the sample. The data were fit using the μSRFIT software package [20].

Electronic band-structure calculations were performed using the DFT method with the linearized augmented plane waves (LAPW) as a basis, as implemented in the WIEN2K code [21]. The generalized gradient approximation (GGA) was used to account for the exchange and correlations [22]. We used a $20 \times 20 \times 20$ \mathbf{k} -point grid to sample the full Brillouin zone.

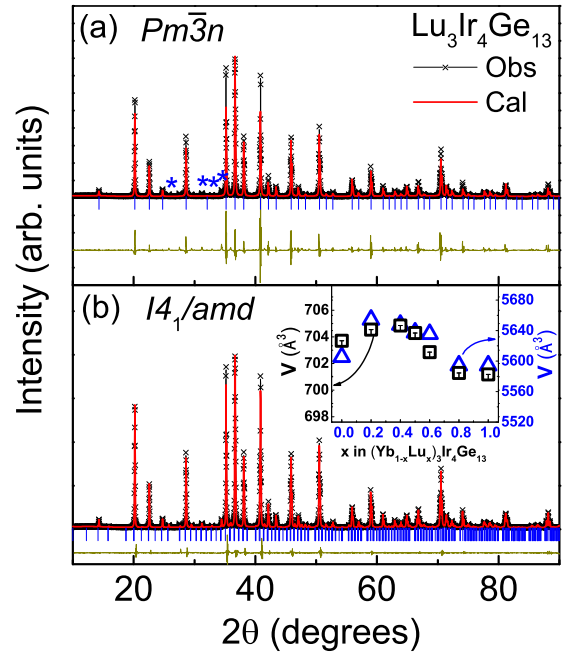


FIG. 1. Room-temperature measured (black symbols) and calculated (red line) powder x-ray diffraction pattern for $\text{Lu}_3\text{Ir}_4\text{Ge}_{13}$, together with the calculated peak positions (blue vertical lines) using space group (a) cubic, $Pm\bar{3}n$ and (b) tetragonal, $I4_1/amd$. The tetragonal model fully accounts for the weak reflections [blue asterisks in (a)] that are unaccounted for in the cubic average model. Inset: variation of lattice parameters as a function of x in $(\text{Yb}_{1-x}\text{Lu}_x)_3\text{Ir}_4\text{Ge}_{13}$ with a (small) cubic unit-cell model (left axis) and a (large) tetragonal unit-cell model (right axis).

III. RESULTS AND DISCUSSIONS

A. Crystallography

When using the cubic $Pm\bar{3}n$ space group, which is adopted in a $\text{Yb}_3\text{Rh}_4\text{Ge}_{13}$ structure type, we observed weak and unindexed reflections in both powder and single-crystal x-ray diffraction patterns [see the asterisks in Fig. 1(a)]. In the case of $\text{Lu}_3\text{Ir}_4\text{Ge}_{13}$, a tetragonal unit cell with cell dimensions $a = 17.7674(11)$ Å and $c = 17.8229(13)$ Å and space group $I4_1/amd$ account for the weaker reflections and peak splitting of major reflections [Fig. 1(b)]. This model was then used to fit the powder diffraction data for $\text{Yb}_3\text{Ir}_4\text{Ge}_{13}$. Rietveld refinement of the data resulted in a model in good agreement with lattice parameters $a = 17.74828(15)$ Å and $c = 17.7894(2)$ Å ($R_{\text{wp}} = 7.08\%$), indicating $\text{Lu}_3\text{Ir}_4\text{Ge}_{13}$ and $\text{Yb}_3\text{Ir}_4\text{Ge}_{13}$ are isostructural and adopt the tetragonal space group $I4_1/amd$ (see details in Ref. [10]). The volume trend as a function of dopants remains the same regardless of unit-cell size, as shown in the inset of Fig. 1(b).

B. Electrical transport properties

Most $4f$ magnetic systems are metallic [1], while the electrical resistivity ρ of YbIG [red symbols, Fig. 2(a)] shows nonmetallic behavior even at high temperatures (temperature is much higher than the Kondo temperature T_K). This cannot be due to incoherent scattering of the conduction electrons by localized f moments, since nonmagnetic LIG exhibits similar

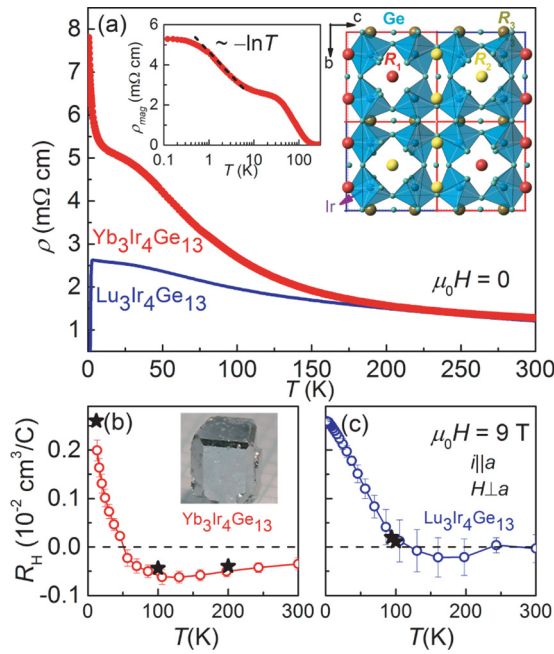


FIG. 2. (a) Zero-field temperature-dependent electrical resistivity ρ of $R_3\text{Ir}_4\text{Ge}_{13}$, $R = \text{Yb}$ and Lu . A sudden drop of $\rho(T)$ in $\text{Lu}_3\text{Ir}_4\text{Ge}_{13}$ is due to a superconducting transition at 2.8 K. The left inset shows a semilogarithmic plot of magnetic electrical resistivity $\rho_{\text{mag}} = \rho_{\text{YbIG}} - \rho_{\text{LIG}}$. The right inset shows the crystal structure of $R_3\text{Ir}_4\text{Ge}_{13}$. Parts (b) and (c) show temperature-dependent Hall coefficients $R_H(T)$ measured at $\mu_0 H = 9$ T for $\text{Yb}_3\text{Ir}_4\text{Ge}_{13}$ and $\text{Lu}_3\text{Ir}_4\text{Ge}_{13}$, respectively. Black stars are data measured in a field sweep mode at a constant T . The error bar represents a difference between cooling and warming measurements. A picture of a crystal is shown in the inset of (b).

$d\rho/dT < 0$ behavior [blue line, Fig. 2(a)]. Below 150 K, the magnetic resistivity $\rho_{\text{mag}} = \rho_{\text{YbIG}} - \rho_{\text{LIG}}$, as shown in the inset of Fig. 2(a), increases with decreasing temperature, implying the opening of some pseudogap in the underlying electronic band structure. Upon cooling below 10 K, ρ_{mag} follows $-\ln T$ behavior, which is a signature of incoherent Kondo scattering. Below 0.9 K, ρ_{mag} tends to saturate due to some loss of spin disorder when magnetic correlations set in. We will discuss the magnetic properties of YbIG in detail later in Sec. III E. On the other hand, in LIG a monotonic increase of $\rho(T)$ is observed down to 2.8 K, below which LIG becomes superconducting (see the Appendix). Similar semiconducting $\rho(T)$ behavior in LIG has recently also been reported by Kumar *et al.* [23]. However, they grew the crystal by using the Czochralski method and reported a different crystal structure $Pm\bar{3}n$. This reflects the fact that reaction conditions and synthesis methods could lead to slightly different polymorphs.

The Hall coefficient data $R_H(T)$ for YbIG are shown down to 16 K (above T_K), below which the anomalous Hall effect dominates [Fig. 2(b)], while the data for LIG are shown down to 2 K [Fig. 2(c)]. The Hall resistance $\rho_H(H)$ was measured at several temperatures, and the R_H values, obtained from linear fits [black stars in Figs. 2(b) and 2(c)], are consistent with the $R_H(T)$ data. A sign change of $R_H(T)$ indicates a change in

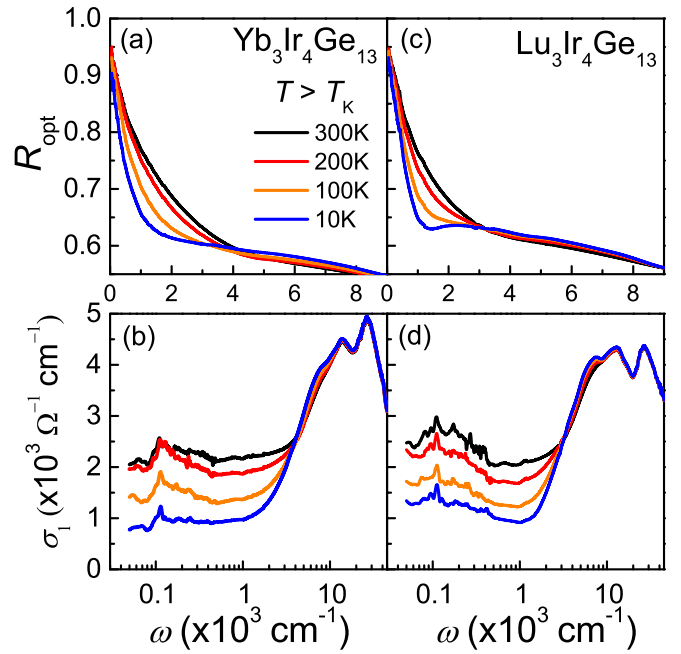


FIG. 3. Optical reflectance R_{opt} and optical conductivity σ_1 as a function of frequency ω of $\text{Yb}_3\text{Ir}_4\text{Ge}_{13}$ (a,b) and $\text{Lu}_3\text{Ir}_4\text{Ge}_{13}$ (c,d) at different temperatures $T = 10, 100, 200,$ and 300 K.

effective carrier type from electrons at high temperatures to holes at low temperatures for both systems.

C. Optical conductivity

Such a gap feature, however, is not seen in our optical conductivity data. Overall, similar optical properties are registered for YbIG [Figs. 3(a) and 3(b)] and LIG [Figs. 3(c) and 3(d)], in both the optical reflectance $R_{\text{opt}}(\omega)$ and the real part of the optical conductivity $\sigma_1(\omega)$. Note that all data for YbIG are taken at $T > T_K \sim 3.5$ K, estimated by specific-heat measurements. Both compounds show a nominally metallic frequency dependence at all measured temperatures: $R_{\text{opt}}(\omega)$ at low energy increases rapidly with decreasing frequency and approaches unity in the zero-frequency limit. As a result, a reflectance edge, though overdamped, is seen in the measured $R_{\text{opt}}(\omega)$ below 4000 cm^{-1} , and a Drude-like peak is seen at low frequency in the $\sigma_1(\omega)$ spectra. For both compounds, the low-frequency reflectance $R_{\text{opt}}(\omega)$ values decrease with decreasing temperature [Figs. 3(a) and 3(c)], leading to a drop of the conductivity in the low-frequency regime. The temperature dependence of $\sigma_1(\omega)$ for YbIG and LIG is consistent with the semimetal-like evolution of $\rho(T)$. A striking observation is that the reflectance edge is located at a rather low energy [$\omega = (3-4) \times 10^3$ cm^{-1}] compared with ordinary metals, indicating that both compounds have very low plasma frequencies or carrier densities. The estimated values of the plasma frequency at 10 K are 4.8×10^3 cm^{-1} for YbIG and 5.7×10^3 cm^{-1} for LIG, which correspond to small carrier densities $n \approx 2.6 \times 10^{20} (m^*/m_e) \text{cm}^{-3}$ for YbIG and $\approx 3.6 \times 10^{20} (m^*/m_e) \text{cm}^{-3}$ for LIG, where m^* is the effective mass and m_e is the free-electron mass. Furthermore, the low-frequency spectral weight is suppressed with decreasing

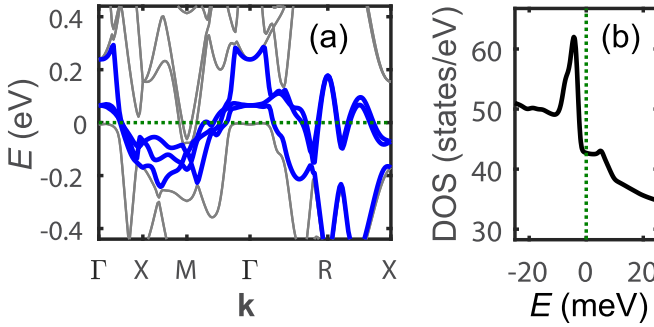


FIG. 4. (a) DFT band structure of $\text{Lu}_3\text{Ir}_4\text{Ge}_{13}$, showing the bands in the vicinity of the Fermi level along the high-symmetry directions. The blue indicates the three bands that cross the Fermi level and contribute most to the carrier density. (b) Corresponding density of states (DOS), exhibiting a narrow van Hove singularity about 4 meV below the Fermi level.

temperature, leading to the formation of a minimum of σ_1 with an energy scale of about 1000 cm^{-1} for both compounds.

D. DFT calculations

To substantiate the conclusion of the low-carrier nature of YbIG and LIG, we have performed the density-functional theory (DFT) calculations, focusing on LIG, where the absence of f -electron bands near the Fermi level allows us to better understand the underlying mechanism for low-carrier density. Shown in Fig. 4(a) is the band structure plotted along high-symmetry lines in the Brillouin zone, from which it follows that there are a total of five pseudospin degenerate bands that cross the Fermi level. Of these five bands, the most significant ones are two holelike bands and one electronlike band, whereas the remaining two electronlike bands form tiny electron pockets near the M point and contribute very little to the carrier density [see Fig. 4(a)]. The individual band carrier densities are summarized in Table I, with the total carrier density equal to $1.91 \times 10^{21} \text{ cm}^{-3}$. This value matches well with the density inferred from the optical conductivity, provided the average effective mass $m^* \approx 5m_e$. Calculations of the effective masses from DFT are unavailable, given the multiple bands and their nonparabolic nature near the Fermi level. Nevertheless, the semiquantitative agreement with the optical data is encouraging. Within the DFT framework, we find that LIG is a fully compensated semimetal, with an equal total number of electronlike and holelike carriers. The band structure contains a nearly flat band close to the Γ point, which nearly touches the Fermi level. This band contributes to a van Hove singularity in the density of states (DOS), at $\approx 4 \text{ meV}$ below the chemical potential, as shown in Fig. 4(b). This finding indicates that LIG should be very sensitive to

TABLE I. Carrier densities corresponding to the dominant holelike and electronlike bands crossing the Fermi level calculated using DFT.

Bands	h1	h2	e1	e2	e3
Carrier density ($\times 10^{20} \text{ cm}^{-3}$)	1.96	7.61	9.43	0.12	0.01

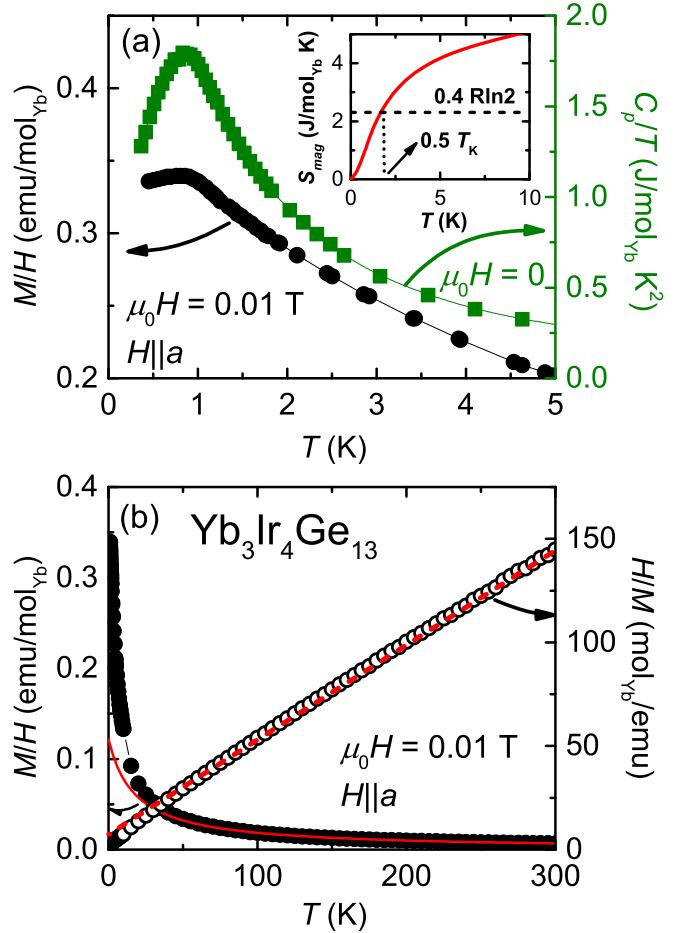


FIG. 5. (a) Low- T M/H vs T (left, circle) and zero-field specific heat C_p/T vs T (right, square) of $\text{Yb}_3\text{Ir}_4\text{Ge}_{13}$. The inset shows the temperature dependence of magnetic entropy S_{mag} , which is calculated from the $4f$ -moment contribution to the specific heat. (b) Magnetic susceptibility M/H vs T (left), where M is the magnetization and H is the magnetic field, and inverse magnetic susceptibility H/M vs T (right) of $\text{Yb}_3\text{Ir}_4\text{Ge}_{13}$. The solid and dashed lines show a Curie-Weiss fit. Note that $1 \text{ emu} = 1 \text{ G cm}^3 = 10^{-3} \text{ A m}^2$.

hole doping; the DOS at the Fermi level could be increased by about 50% if the chemical potential were shifted to coincide with the van Hove peak. Such a substantial enhancement of the DOS signals that this system may have a propensity toward magnetic ordering, based on a Stoner criterion-type argument.

E. Magnetic properties and μSR measurements

We have so far demonstrated the low-carrier-density properties of YbIG and LIG, and we turn next to the magnetic properties of YbIG. The single-ion Kondo temperature $T_K \approx 3.5 \text{ K}$ for YbIG, which is estimated from the magnetic entropy, i.e., $S_{\text{mag}}(0.5T_K) = 0.4R \ln 2$ [inset of Fig. 5(a)], implies that above $T = 50 \text{ K}$, YbIG can be regarded as a local-moment system. Indeed, an effective moment $\mu_{\text{eff}}^{\text{exp}} = 4.2 \mu_B/\text{mol}_{\text{Yb}}$, close to the Yb^{3+} free-ion value of $\mu_{\text{eff}}^{\text{calc}} = 4.54 \mu_B/\text{mol}_{\text{Yb}}$, is obtained from the Curie-Weiss fit of the inverse magnetic susceptibility H/M [open symbols, right axis in Fig. 5(b)]. The

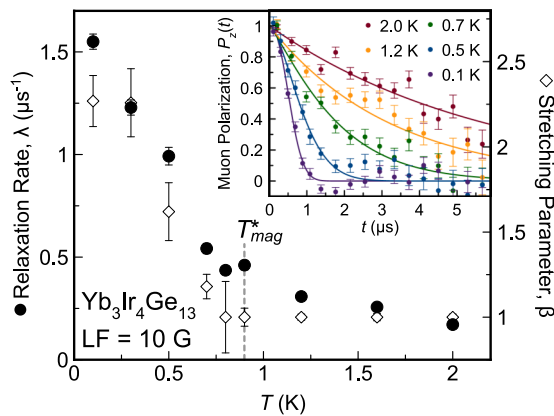


FIG. 6. Temperature dependence of the muon spin relaxation rate, λ (filled circles), and the stretching parameter, β (open diamonds), for $\text{Yb}_3\text{Ir}_4\text{Ge}_{13}$, indicating a magnetic response correlated with $T^* = 0.9$ K. Inset: selection of representative μSR spectra, where the solid lines are the fits to the data with a stretched exponential function. The error bars represent one standard deviation.

fit results in a Weiss temperature $\theta_W = -18$ K, suggesting antiferromagnetic correlations. Upon further cooling, these antiferromagnetic correlations result in a phase-transition-like feature at $T_{\text{mag}}^* = 0.9$ K as seen from the peaks in M/H (circles, left axis) and C_p/T (squares, right axis) shown in Fig. 5(a), and the local minimum in $d\rho/dT$ (not shown). However, the magnetism appears to be very fragile, as indicated by the neutron diffraction and muon spin relaxation (μSR) measurements discussed next. While neutron diffraction measurements (not shown) clearly observe the diffraction pattern of the crystal structure, no magnetic peaks were found down to 80 mK. This might reflect the fact that the ordered moment of YbIG below T_{mag}^* is smaller than can be resolved from neutron diffraction (typically $\leq 0.1\mu_B$).

To better understand the nature of the magnetic state in YbIG below $T_{\text{mag}}^* = 0.9$ K, we performed μSR measurements between 0.1 and 2 K. Several representative muon polarization spectra are presented in the inset of Fig. 6. As the sample is cooled below T_{mag}^* , there are no spontaneous oscillations in the decay asymmetry. However, there is a continuous evolution in the asymmetry that is well described by a phenomenological stretched exponential function,

$P_z(t) = \exp(-\lambda t)^\beta$, where λ is the relaxation rate and β is the stretching parameter. The temperature dependence of the fitted parameters λ and β is presented in Fig. 6. Above T_{mag}^* , the stretching parameter is close to $\beta = 1$ and the relaxation rate is relatively small, less than $0.5 \mu\text{s}^{-1}$. As the sample is cooled below T_{mag}^* , both the relaxation rate and the stretching parameter increase monotonically down to the lowest measured temperature, 0.1 K. The increase in the relaxation rate indicates a continuous slowing of the Yb^{3+} spin fluctuations. Our recent inelastic neutron scattering measurements on YbIG down to 0.6 K reveal nontrivial dynamic magnetic correlations between Yb moments [24]. At 0.1 K, most of the moments become static on the muon timescale, as evidenced by $\beta \approx 2$. Thus, it is clear that, though fragile, the T_{mag}^* feature has a magnetic origin.

At first glance, the sister compound $\text{Ce}_3\text{Co}_4\text{Sn}_{13}$ might appear synonymous with YbIG: specific-heat measurements reveal a broad peak at 0.8 K in $\text{Ce}_3\text{Co}_4\text{Sn}_{13}$ [25,26] below which elastic neutron scattering data do not show signs of long-range magnetic order [27], even though inelastic neutron scattering data reveal antiferromagnetic correlations below 15 K [28]. However, the electrical resistivity data on polycrystalline and single crystalline $\text{Ce}_3\text{Co}_4\text{Sn}_{13}$ show a sample dependence [26,29,30], and the infrared spectroscopy study on the single crystalline sample indicates good metallic response [31], unlike the present evidence for low-carrier semimetallic behavior in YbIG and its nonmagnetic analog LIG. Therefore, the fragile magnetism in YbIG and $\text{Ce}_3\text{Co}_4\text{Sn}_{13}$ are likely of different origins.

F. Substitution series $(\text{Yb}_{1-x}\text{Lu}_x)_3\text{Ir}_4\text{Ge}_{13}$

Next we study the substitution series $(\text{Yb}_{1-x}\text{Lu}_x)_3\text{Ir}_4\text{Ge}_{13}$ (YLIG) to further explore the fragile magnetism of YbIG. From $d\rho/dT$, C_p/T , and M/H we summarized T_{mag}^* values as a function of x in YLIG, as shown in Fig. 7(d). Increasing x gradually reduces T_{mag}^* to zero temperature at the critical composition $x_c \sim 0.6$. The broad hump around 40 K in ρ_{mag} for YbIG, which originates from the opening of some pseudogap in the underlying electronic band structure [Fig. 2(a)], gradually vanishes with increasing x [Fig. 7(a)], because $x = 0.6-0.7$ ρ_{mag} is not observed to saturate and instead obeys $\rho_{\text{mag}} \sim -\ln T$ from 10 K down to the lowest measured temperature. Because of the underlying semimetallic

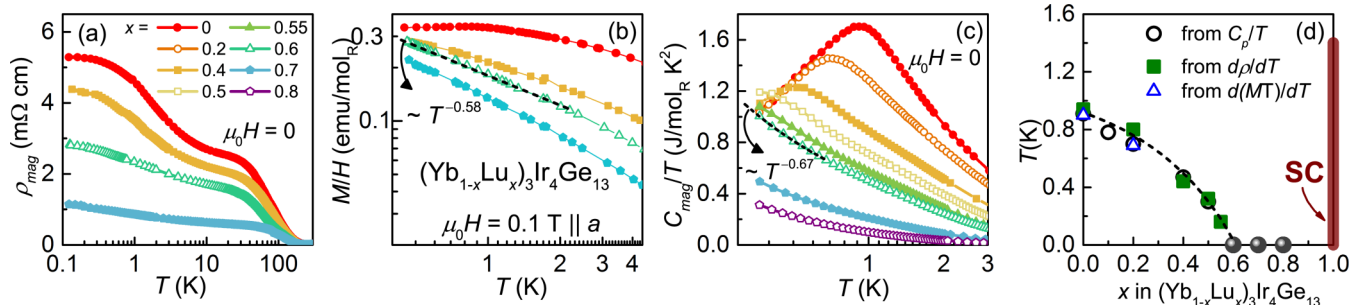


FIG. 7. (a) Zero-field temperature-dependent magnetic electrical resistivity ρ_{mag} of $(\text{Yb}_{1-x}\text{Lu}_x)_3\text{Ir}_4\text{Ge}_{13}$. (b) Low-temperature magnetic susceptibility M/H vs T at $\mu_0 H = 0.01 \text{ T} \parallel a$ axis. (c) Zero-field magnetic specific heat C_{mag}/T of $(\text{Yb}_{1-x}\text{Lu}_x)_3\text{Ir}_4\text{Ge}_{13}$ with conduction-electron and phonon contributions being subtracted. (d) T vs Lu concentration, x , phase diagram. The dashed line separates the low- T fragile magnetic state. SC stands for the superconducting state for LIG.

TABLE II. The exponent λ obtained from $M/H \sim T^{\lambda-1}$ and $C_{\text{mag}}/T \sim T^{\lambda-1}$ for $x = 0.55-0.7$ in $(\text{Yb}_{1-x}\text{Lu}_x)_3\text{Ir}_4\text{Ge}_{13}$.

x in $(\text{Yb}_{1-x}\text{Lu}_x)_3\text{Ir}_4\text{Ge}_{13}$	0.55	0.6	0.7
λ in $M/H \sim T^{\lambda-1}$	0.58	0.42	0.36
λ in $C_{\text{mag}}/T \sim T^{\lambda-1}$	0.42	0.32	0.17

character, this cannot be directly compared with metallic diluted Kondo systems, where a Kondo minimum is observed in the resistivity [32]. The magnetic susceptibility M/H and the magnetic specific heat, $C_{\text{mag}}/T = C/T(\text{YLIG}) - C/T(\text{LIG})$, both show a power-law temperature dependence close to x_c [Figs. 7(b) and 7(c), respectively]. This behavior is reminiscent of the exotic infinite-randomness quantum critical point accompanied by a quantum Griffiths phase, which results in power-law singularities of thermodynamic observables, e.g., $C/T \sim M/H \sim T^{\lambda-1}$ (Ref. [33]). The values of the exponent λ obtained from specific heat and magnetic susceptibility for $x = 0.55-0.7$ in YLIG are summarized in Table II. However, these values are not consistent with the predicted trend of λ for a Griffiths phase, where $\lambda = 0$ at the quantum critical point and it increases moving away from the critical point [34]. A Griffiths phase is formed by chemical substitution of a nonmagnetic element into a parent compound with long-range magnetic order. Therefore, the fact that our parent compound, YbIG, does not exhibit long-range magnetic order implies that the power-law dependence of C/T and M/H is only of some relevance to the physics of the Griffiths phase.

A recent theoretical model is aimed at describing the dilute-carrier Kondo limit in a honeycomb lattice [17]. In this context, the crystallographic details of YbIG become relevant: Given the even number of Yb atoms/sites (48) in one unit cell [inset of Fig. 2(a)], YbIG has the structural framework for which to employ the even-site-per-unit-cell Kondo-lattice model in the dilute-carrier limit. The theoretical study of such a model has shown that the Kondo effect in this regime gives rise to semimetallic behavior [17]. Although the theoretical model describes a honeycomb lattice symmetry instead of the tetragonal crystal system observed here, the essential physics of the even-site low-carrier framework is unambiguously the same. The $\rho(T)$ behavior we have observed in the low-temperature regime of YbIG is compatible with this mechanism. At the same time, the RKKY interaction in this regime is expected to be long-ranged and thus inherently frustrated. This renders the fragile magnetism we have observed in YbIG a rather natural consequence. As such, we have not only discovered another regime of the Kondo effect and magnetic correlations in YbIG, but our work has also revealed how such effects can be tuned through the Lu-for-Yb substitution in YLIG, leading to Griffiths-phase-like properties.

IV. SUMMARY

In summary, YbIG is a low-carrier semimetal with Kondo behavior arising from a low-carrier *nonmagnetic* reference compound, LIG, and it displays fragile magnetism. The complex intertwinement of low-carrier character and magnetism in YLIG may lead to an exploration of the strong correlation effects in a semimetallic environment.

ACKNOWLEDGMENTS

We thank B. S. Hitti for assistance with the μSR measurements, and J. M. Santiago for assistance with the neutron diffraction measurements. We thank K. Iwasa and M. S. Foster for fruitful discussions. B.K.R., C.-L.H., and E.M. acknowledge support from the Gordon and Betty Moore Foundation EPIQS Initiative through Grant No. GBMF 4417. N.L.W. is supported by the National Science Foundation of China (No. 11888101) and the National Key Research and Development Program of China (No. 2016YFA0300902 and No. 2017YFA0302904). A.M.H., M.N.W., and G.M.L. acknowledge support from NSERC of Canada. The neutron scattering work at Rice is supported by the U.S. DOE, BES under Contract No. DE-SC0012311 (P.D.). A part of the material characterization work at Rice is supported by the Robert A. Welch Foundation Grant No. C-1839 (P.D.). The theoretical work at Rice University was supported by NSF CAREER Grant No. DMR-1350237 (A.H.N.) and the Robert A. Welch Foundation Grant No. C-1818 (V.L. and A.H.N.), as well as by the NSF Grant No. DMR-1611392 and the Robert A. Welch Foundation Grant No. C-1411 (Q.S.), with travel support provided by the ARO Grant No. W911NF-14-1-0525. UT Dallas acknowledges support from NSF DMR-1700030. S.D. acknowledges Junior Short Award ICAM-I2CAM QuantEmX scientific report. S.D. and S.P. gratefully acknowledge financial support from the Austrian Science Funds (FWF doctoral program W1243 and FWF I2535-N27) and the U.S. Army research office (Grant No. W911NF-14-1-0496). The identification of any commercial product or trade name does not imply endorsement or recommendation by the National Institute of Standards and Technology.

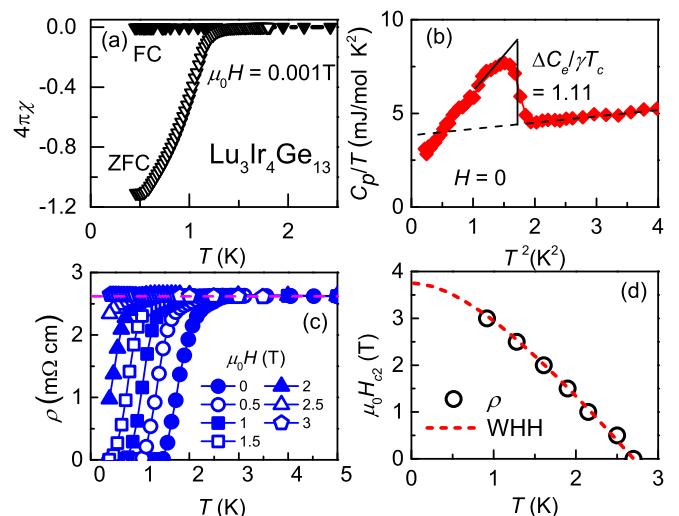


FIG. 8. Superconducting properties of $\text{Lu}_3\text{Ir}_4\text{Ge}_{13}$. (a) Zero-field-cooled (ZFC) and field-cooled (FC) magnetic susceptibility as a function of temperature at $\mu_0 H = 0.001$ T. (b) Zero-field specific heat C_p/T vs T^2 . The dashed line is the normal-state contribution. Two solid lines indicate local entropy conservation from which dimensionless $\Delta C_e/\gamma T_c$ is determined. (c) Low-temperature resistivity with various magnetic fields. The violet dashed line represents the normal-state resistivity. (d) Critical field $\mu_0 H_{c2}$ vs T_c^{0n} plot. The red dashed line is a theoretical WHH curve.

APPENDIX

Figure 8 shows the low-temperature data of $\text{Lu}_3\text{Ir}_4\text{Ge}_{13}$ to demonstrate its superconductivity with a transition temperature of 1.4 K. The dimensionless $\Delta C_e/\gamma T_c = 1.11$ suggests that the superconductivity of $\text{Lu}_3\text{Ir}_4\text{Ge}_{13}$ is in the weak-coupling regime. From the resistivity $\rho(T)$ plot in

different fields, we determine the values of T_c^{on} below which ρ deviates from its normal-state value [dashed line in Fig. 8(c)]. The critical field $\mu_0 H_{c2}$ versus T_c^{on} plot is shown in Fig. 8(d), where $\mu_0 H_{c2}(T_c^{\text{on}})$ can be well described by the conventional Werthamer-Helfand-Hohenberg (WHH) theory, implying BCS-like superconductivity in $\text{Lu}_3\text{Ir}_4\text{Ge}_{13}$.

-
- [1] G. Stewart, *Rev. Mod. Phys.* **73**, 797 (2001).
- [2] C. Pfleiderer, *Rev. Mod. Phys.* **81**, 1551 (2009).
- [3] T. Takabatake, F. Iga, T. Yoshino, Y. Echizen, K. Katoh, K. Kobayashi, M. Higa, N. Shimizu, Y. Bando, G. Nakamoto, H. Fujii, K. Izawa, T. Suzuki, T. Fujita, M. Sera, M. Hiroi, K. Maezawa, S. Mock, H. V. Löhneysen, A. Brückl, K. Neumaier, and K. Andres, *J. Magn. Magn. Mater.* **177–181**, 277 (1998).
- [4] Q. Si and F. Steglich, *Science* **329**, 1161 (2010).
- [5] T. Takabatake, G. Nakamoto, T. Yoshino, H. Fujii, K. Izawa, S. Nishigori, H. Goshima, T. Suzuki, T. Fujita, K. Maezawa, T. Hiraoka, Y. Okayama, I. Oguro, A. A. Menovsky, K. Neumaier, A. Brückl, and K. Andres, *Physica B* **223**, 413 (1996).
- [6] S. Nishigori, H. Goshima, T. Suzuki, T. Fujita, G. Nakamoto, H. Tanaka, T. Takabatake, and H. Fujii, *J. Phys. Soc. Jpn.* **65**, 2614 (1996).
- [7] Y. Luo, F. Ronning, N. Wakehama, X. Lu, T. Park, Z.-A. Xu, and J. D. Thompson, *Proc. Natl. Acad. Sci. (USA)* **112**, 13520 (2015).
- [8] S. Dzsaber, L. Prochaska, A. Sidorenko, G. Eguchi, R. Svagera, M. Waas, A. Prokofiev, Q. Si, and S. Paschen, *Phys. Rev. Lett.* **118**, 246601 (2017).
- [9] B. K. Rai, I. W. H. Oswald, J. K. Wang, G. T. McCandless, J. Y. Chan, and E. Morosan, *Chem. Mater.* **27**, 2488 (2015).
- [10] I. W. H. Oswald, B. K. Rai, G. T. McCandless, E. Morosan, and J. Chan, *Cryst. Eng. Commun.* **19**, 3381 (2017).
- [11] B. K. Rai, I. W. H. Oswald, J. Y. Chan, and E. Morosan, *Phys. Rev. B* **93**, 035101 (2016).
- [12] S. K. Malik, L. Menon, K. Ghosh, and S. Ramakrishnan, *Phys. Rev. B* **51**, 399 (1995).
- [13] Y. Echizen, K. Umeo, and T. Takabatake, *Solid State Commun.* **111**, 153 (1999).
- [14] Y. Luo, J. Bao, C. Shen, J. Han, X. Yang, C. Lv, Y. Li, W. Jiao, B. Si, C. Feng, J. Dai, G. Cao, and Z.-A. Xu, *Phys. Rev. B* **86**, 245130 (2012).
- [15] F. F. Tafti, Q. D. Gibson, S. K. Kushwaha, N. Hal-dolaarachchige, and R. J. Cava, *Nat. Phys.* **12**, 272 (2016).
- [16] S. Sun, Q. Wang, P.-J. Guo, K. Liu, and H. Lei, *New J. Phys.* **18**, 082002 (2016).
- [17] X.-Y. Feng, H. Zhong, J. Dai, and Q. Si, [arXiv:1605.02380](https://arxiv.org/abs/1605.02380).
- [18] J. W. Lynn, Y. Chen, S. Chang, Y. Zhao, S. Chi, W. Ratcliff, II, B. G. Ueland, and R. W. Erwin, *J. Res. NIST* **117**, 61 (2012).
- [19] S. J. Blundell, *Contemp. Phys.* **40**, 175 (1999).
- [20] A. Suter and B. Wojek, *Phys. Proc.* **30**, 69 (2012).
- [21] P. Blaha, K. Schwarz, G. Madsen, D. Kvasnicka, and J. Luitz, *An Augmented Plane Wave + Local Orbitals Program for Calculating Crystal Properties* (Vienna University of Technology, Vienna, Austria, 2001).
- [22] J. P. Perdew, K. Burke, and M. Ernzerhof, *Phys. Rev. Lett.* **77**, 3865 (1996).
- [23] A. Kumar, S. Matteppanavar, A. Thamizhavel, and S. Ramakrishnan, *DAE Solid State Physics Symposium 2017*, AIP Conf. Proc. No. 1942 (AIP, New York, 2018), p. 130060.
- [24] K. Iwasa, C.-L. Huang, B. K. Rai, E. Morosan, S. Ohira-Kawamura, and K. Nakajima, [arXiv:1810.11238](https://arxiv.org/abs/1810.11238).
- [25] A. L. Cornelius, A. D. Christianson, J. L. Lawrence, V. Fritsch, E. D. Bauer, J. L. Sarrao, J. D. Thompson, and P. G. Pagliuso, *Physica B* **378**, 113 (2006).
- [26] A. Slebarski, B. D. White, M. Fijalkowski, J. Goraus, J. J. Hamlin, and M. B. Maple, *Phys. Rev. B* **86**, 205113 (2012).
- [27] A. D. Christianson, J. S. Gardner, H. J. Kang, J.-H. Chung, S. Bobev, J. L. Sarrao, and J. M. Lawrence, *J. Magn. Magn. Mater.* **310**, 266 (2007).
- [28] K. Iwasa, Y. Otomo, K. Suyama, K. Tomiyasu, S. Ohira-Kawamura, K. Nakajima, and J.-M. Mignot, *Phys. Rev. B* **95**, 195156 (2017).
- [29] E. L. Thomas, H.-O. Lee, A. N. Bankston, S. MaQuilon, P. Klavins, M. Moldovan, D. P. Young, Z. Fisk, and J. Y. Chan, *J. Solid State Chem.* **179**, 1642 (2006).
- [30] C. S. Lue, H. F. Liu, S. L. Hsu, M. W. Chu, H. Y. Liao, and Y. K. Kuo, *Phys. Rev. B* **85**, 205120 (2012).
- [31] W. J. Ban, J. L. Luo, and N. L. Wang, *J. Phys.: Condens. Matter* **29**, 405603 (2017).
- [32] K. Winzer, *Solid State Commun.* **16**, 521 (1975).
- [33] T. Vojta and J. Schmalian, *Phys. Rev. B* **72**, 045438 (2005).
- [34] S. Ubaid-Kassis, T. Vojta, and A. Schroeder, *Phys. Rev. Lett.* **104**, 066402 (2010).